



Nonperturbative study of bulk photovoltaic effect enhanced by an optically induced phase transitionSangeeta Rajpurohit ^{1,*}, C. Das Pemmaraju,² Tadashi Ogitsu,³ and Liang Z. Tan ¹¹*Molecular Foundry, Lawrence Berkeley National Laboratory, Berkeley, California 94720, USA*²*Stanford Institute for Materials & Energy Sciences, SLAC National Accelerator Laboratory, Menlo Park, CA 94025, USA*³*Lawrence Livermore National Laboratory, Livermore, California 94550, USA*

(Received 24 May 2021; revised 7 January 2022; accepted 16 February 2022; published 16 March 2022)

Solid systems with strong correlations and interactions under light illumination have the potential for exhibiting interesting bulk photovoltaic behavior in the nonperturbative regime, which has remained largely unexplored in past theoretical studies. We investigate the bulk photovoltaic response of a perovskite manganite with strongly coupled electron-spin-lattice dynamics using real-time simulations performed with a tight-binding model. The transient changes in the band structure and the photoinduced phase transitions, emerging from spin and phonon dynamics, result in a nonlinear current versus intensity behavior beyond the perturbative limit. The current rises sharply across a photoinduced magnetic phase transition, which later saturates at higher light intensities due to excited phonon and spin modes. The predicted peak photoresponsivity is an order of magnitude higher than another known transition metal ferroelectric oxide BiFeO₃. We disentangle phonon- and spin-assisted components to the ballistic photocurrent, showing that they are comparable in magnitude. Our results illustrate a promising alternative way for controlling and optimizing the bulk photovoltaic response through the photoinduced phase transitions in strongly correlated systems.

DOI: [10.1103/PhysRevB.105.094307](https://doi.org/10.1103/PhysRevB.105.094307)**I. INTRODUCTION**

The bulk photovoltaic effect (BPVE) is the generation of photocurrent in the bulk of a material, in the absence of any extrinsic carrier separation mechanism such as heterojunctions, and arising purely from its intrinsic noncentrosymmetry [1–3]. As BPVE is not subject to the usual constraints of conventional p-n junction photovoltaics, such as the Shockley-Queisser limit, it has promising applications in next-generation light-harvesting and sensing as well as connections to band-structure topology [4–7]. Shift currents and phonon-induced ballistic currents are two main mechanisms that have been put forward to explain BPVE in recent years with relative magnitudes that are strongly dependent on crystal structure and materials system. Shift currents [8–15] arise from the asymmetry of the nonlinear interactions of carriers with the light field. The ballistic currents are caused by the asymmetry of the momentum distributions of charge carriers [16–18] in noncentrosymmetric materials.

Complex materials with tuneable interactions and correlations are a promising class of systems to control and optimize the BPVE. Previous theoretical studies of BPVE are mostly based on perturbative methods [13,14,18–21]. The validity of these theories in the nonperturbative regime is unclear where charge dynamics is strongly coupled to phonon and spin dynamics. In this paper, we take a nonperturbative approach for studying the BPVE to investigate its behavior in a strongly correlated system as light intensity is increased continuously

from the perturbative regime to current saturation. While perturbative calculations of the shift and ballistic currents are mostly performed by keeping the band structure and scattering matrix of carriers fixed, this rigid-band approximation can potentially break down as the light intensity is increased. For instance, electron-phonon interactions can result in deviations from lowest-order behavior [20,22]. This is of particular relevance for strongly correlated systems with charge carriers dressed in the form of excitons, polarons, and magnons [23–29]. To include the dynamical effects [30,31] arising due to the changes in the local symmetries and the band structure, we simulate the real-time evolution of the electron, spin, and lattice degrees of freedom.

We study the BPVE of a strongly correlated perovskite manganite $A_{1-x}A'_x\text{MnO}_3$ ($A=\text{La, Pr, and } A'=\text{Ca}$) at doping $x = 2/3$ [32–34]. In its ground state, this system is in a bistrife (BS) phase and is an improper ferroelectric with a weak polarization, exhibiting charge order (CO) and orbital order (OO). We report that its photocurrent has a strongly nonlinear dependence on intensity stemming from a photoinduced magnetic phase transition that occurs during the optical excitation itself. Couplings to charge, spin, and phonon degrees of freedom are each necessary for this photoinduced phase transition. These results show that the consideration of phonon and spin dynamics is necessary for designing materials with tunable BPVE properties.

A. Tight-binding model

In $A_{1-x}A'_x\text{MnO}_3$ ($A = \text{rare-earth metal and } A' = \text{alkaline-earth metal}$) manganites, the octahedral crystal field splits the Mn 3d-shell into three nonbonding t_{2g} orbitals and two

*srajpurohit@lbl.gov.

antibonding e_g orbitals. We treat the delocalized e_g orbitals using a tight-binding model and the localized t_{2g} electrons as classical spins \vec{S}_R with length $|\vec{S}| = 3/2$ for each Mn-ion R. The potential energy of the system is expressed as

$$E_{\text{pot}}(|\psi_n\rangle, \vec{S}_R, Q_{i,R}) = E_e(|\psi_n\rangle) + E_S(\vec{S}_R) + E_{\text{ph}}(Q_{i,R}) + E_{e-\text{ph}}(|\psi_n\rangle, Q_{i,R}) + E_{e-S}(|\psi_n\rangle, \vec{S}_R) \quad (1)$$

in terms of one-particle states $|\psi_n\rangle = \sum_{\sigma,\alpha,i} |\chi_{\sigma,\alpha,i}\rangle \psi_{\sigma,\alpha,i,n}$ of e_g electrons, t_{2g} -spin \vec{S}_R , and oxygen octahedral $Q_{i,R}$ phonon modes. The basis set $|\chi_{\sigma,\alpha,i}\rangle$'s for the one-particle states consists of local spin orbitals with spin $\sigma \in \{\uparrow, \downarrow\}$ and the orbital character $\alpha \in d_{x^2-y^2}, d_{3z^2-r^2}$.

The e_g electrons delocalize between Mn sites via intermediate oxygen bridges. The electrons experience an onsite Coulomb interaction, a Hund's coupling from t_{2g} -spin \vec{S}_R , and an electron-phonon (el-ph) coupling with three local phonon modes per Mn site. The phonon modes are the octahedral breathing $Q_{1,R}$ and the two Jahn-Teller (JT) active modes $Q_{2,R}$ and $Q_{3,R}$. These modes are highly cooperative due to the oxygen atoms shared between adjacent MnO_6 octahedra. The t_{2g} -spins \vec{S}_R encounter an antiferromagnetic intersite coupling. For the complete details of the model and its parameters, we refer to Refs. [35–37].

II. RESULTS

We combine a tight-binding model for manganites with Ehrenfest dynamics to study the photocurrent generation and its evolution.

A. Ground state

We predict that the BS phase has a stable noncollinear spin order (SO) in its ground state, illustrated in Fig. 1(a), which is lower in energy than previously reported collinear SOs [38]. The ordering within ab planes can be seen as an arrangement of horizontal and vertical “trimers” which are three almost ferromagnetically aligned Mn-sites, with average spin angles of 5.8° and 34.2° , in a row $\text{Mn}^{4+ \text{ I}} - \text{Mn}^{3+} - \text{Mn}^{4+ \text{ II}}$. There are additional $\text{Mn}^{4+ \text{ III}}$ sites that are not part of trimers. In the \vec{c} direction, the SO is antiferromagnetic. The BS ground state is noncentrosymmetric with a calculated net polarization of 15 nC/cm^2 in the \vec{a} direction (more information in the Supplemental Material). The electronic structure of the BS phase can be explained in terms of Wannier states $|w_i\rangle$ ($i \in \{1, 2, \dots, 6\}$) (details in the Supplemental Material) spanning the Hilbert space of the trimer segments and Mn^{4+} sites; see Fig. 1(d) (more details in the Supplemental Material). The band gap between the occupied $|w_1\rangle$ states and the other unoccupied $|w_i\rangle$ states arises predominantly from the JT splitting at Mn^{3+} sites and is highly sensitive to the octahedral modes. The doubly degenerate $|w_6\rangle$ are two e_g orbitals of $\text{Mn}^{4+ \text{ III}}$ sites. The density of states projected on the $|w_i\rangle$ states, shown in Fig. 1(e), clearly indicates the valence band consists of the bonding state of trimers, i.e., $|w_1\rangle$ states, with maximum weight on the central Mn^{3+} sites. Above the Fermi level are the nonbonding $|w_2\rangle$ states localized on the $\text{Mn}^{4+ \text{ I}}$ and II terminal sites. Under optical excitation, the BS phase

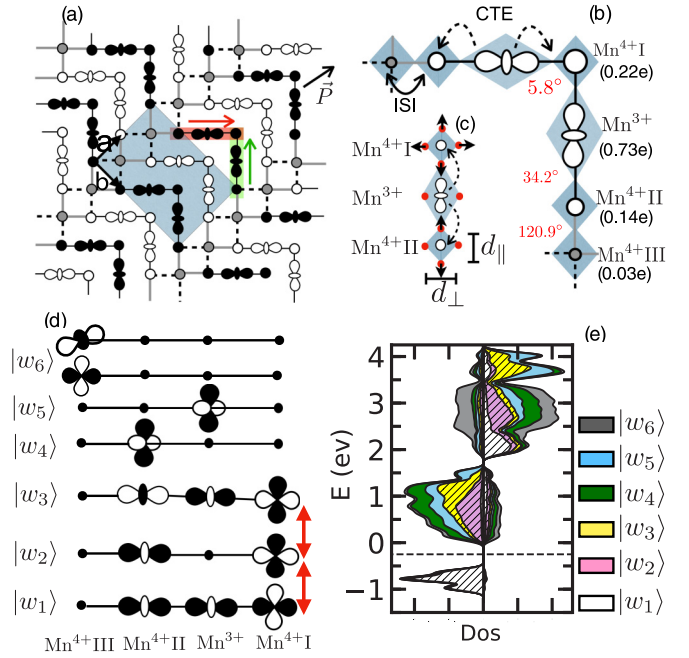


FIG. 1. (a) CO, OO, and SO of BS phase within the ab plane. The circles and $d_{3x^2-r^2}/d_{3z^2-r^2}$ -like orbitals are Mn^{4+} and Mn^{3+} sites, respectively. Black, white, and gray indicate sites with different t_{2g} -spin orientation. The red (green) arrow indicates the local polarization direction of the horizontal (vertical) trimer and the black arrow indicates the net polarization \vec{P} in the ab plane. (b) Enlarged view of a pair of orthogonal adjacent trimer segments $\text{Mn}^{4+ \text{ I}} - \text{Mn}^{3+} - \text{Mn}^{4+ \text{ II}}$ with an additional $\text{Mn}^{4+ \text{ III}}$ site indicating local e_g -electron densities (values in brackets) and intersite spin angles (values in red). The solid and dashed arrows indicate charge transfer excitation (CTE) and photoinduced intersite interaction (ISI). (c) Displacement (shown by arrows) of oxygen ions (red circles) following photo excitation. (d) Nature of Wannier states $|w_i\rangle$ where $i \in \{1, 2, \dots, 6\}$. The oxygen contribution is downfolded and built into the Mn-d orbitals. The red arrows show intertrimer dipole-allowed transitions. (e) Density of states for e_g d states of Mn atoms projected on $|w_i\rangle$ states. The right and left sides show majority- and minority-spin states, respectively, and the dashed line is the Fermi level.

is expected to display two types of intratrimer dipole-allowed transitions: $|w_1\rangle$ to $|w_2\rangle$ and $|w_2\rangle$ to $|w_3\rangle$.

B. Generation and evolution of photocurrent

We study the dynamics of the optically excited system by combining the model in Eq. (1) with Ehrenfest dynamics [36,37]. In the Supplemental Material [39], we benchmark this method against previous perturbation theory results for the shift current in a simple model, showing good agreement in the limit where the perturbation theory is valid. The effect of the light-pulse, which is defined by electric-field $\vec{E}(r, t) = \vec{e}_A \omega \text{Im}(A_0 e^{-i\omega t}) g(t)$, is incorporated in the model by the Peierls substitution method [40]. Here A_0 is the magnitude of the vector potential, ω is the angular frequency, and \vec{e}_A is the direction of the electric field. The pulse shape is Gaussian fixed by $g(t) = e^{-\frac{t^2}{2\tau_0^2}} (\sqrt{\pi} c_\omega^2)^{-1}$ where pulse duration is defined by its FWHM $= 2c_\omega \sqrt{\ln 2}$. The propagation of the

single-particle wave-functions $|\psi_{\sigma,\alpha,R,n}\rangle$ and the spins \vec{S}_R is governed by the time-dependent Schrodinger equation while the atoms are treated classically, and they evolve according to Newton's equations of motion (more information is in the Supplemental Material).

The simulations are performed at temperature $T = 0$ and do not include any temperature effects. The total energy of the system remains conserved during the simulations. However, the el-ph interaction and the electron-spin interaction, defined by E_{e-ph} and E_{e-S} in Eq. (1), respectively, allow energy exchange between electron, spin, and phonon subsystems and therefore act as a friction in the equations of motion. At the Ehrenfest level [41], the forces on the phonon subsystem contain electronic friction, and phonon emission due to forces from optically excited electrons is allowed. Furthermore, electrons can scatter to states of different crystal momenta due to interaction with phonons and spins; this process is required for ballistic currents [18].

To measure the photocurrent magnitude, we calculate the evolution of the current-density $\vec{j}^{el}(t)$ which is defined at time t as $\vec{j}^{el}(t) = -\frac{e}{V} \sum_{l \in N_R} \vec{j}_l(t)$, where $V = d_{Mn-Mn}^3 N_R$ is the volume of the unit cell with N_R number of Mn ions and with average bond length $d_{Mn-Mn} = 3.84 \text{ \AA}$ between Mn ions. The current vector $\vec{j}_l(t)$ at lattice site l is expressed as

$$\vec{j}_l(t) = \sum_n f_n(t) \sum_{l' \in (NN)} \sum_{\sigma} \sum_{\alpha, \beta} \frac{i}{\hbar} (\psi_{\sigma,\alpha,l,n}^*(t) T'_{\alpha,\beta,l,l'} \psi_{\sigma,\beta,l',n}(t) - \psi_{\sigma,\beta,l',n}^*(t) T'_{\beta,\alpha,l,l'} \psi_{\sigma,\alpha,l,n}(t)) d_{Mn-Mn} \vec{e}_{l-l'}. \quad (2)$$

Here $f_n(t)$ is the instantaneous occupation of the one-particle states $|\psi_n\rangle = \sum_{\sigma,\alpha,l} |\chi_{\sigma,\alpha,l}\rangle \psi_{\sigma,\alpha,l,n}(t)$ and $\vec{e}_{l-l'} = \left(\frac{\vec{R}_l - \vec{R}_{l'}}{|\vec{R}_l - \vec{R}_{l'}|} \right)$ is the unit vector in the direction joining sites l and l' . $T'_{\alpha,\beta,l,l'} = T_{\alpha,\beta,l,l'} e^{-i\vec{A}(t) \cdot (\vec{R}_l - \vec{R}_{l'})}$, where $T_{\alpha,\beta,l,l'}$ is the hopping matrix element between e_g -orbitals α and β at sites l and l' , respectively.

We simulate the photocurrent of a $12 \times 12 \times 4$ perovskite supercell under a 100 fs Gaussian pulse and periodic boundary conditions (Γ -point k -point sampling). The photon energy was set at $\hbar\omega_o = 1.03$ eV, where the system shows maximum absorption. Here we discuss results for light polarization in the \vec{a} direction, with light polarization in the \vec{b} direction being qualitatively similar, resulting in photocurrents that are always aligned along the bulk polarization direction. Light polarization in the \vec{c} direction results in no net current because it contains a mirror plane. The current versus intensity behavior over a range of intensities typical of ultrafast spectroscopies separates into three distinct regions [Fig. 2(a)]: Region I ($I = 0 - 0.60$ mJ/cm²) where the current grows linearly with the light intensity; region II ($I = 0.60 - 1.70$ mJ/cm²) with a sharp rise in the photocurrent; region III ($I > 1.70$ mJ/cm²) when the photocurrent saturates.

The current direction in region I is predominantly along the bulk polarization direction, \vec{a} . Spin dynamics are not yet active in this region, with the ground state SO remaining intact and the photoinduced dynamics is entirely driven by electrons and phonons. The electronic transitions in region I are predominantly intratrimer $|w_1\rangle$ to $|w_2\rangle$ and involve the charge transfer from the Mn³⁺ to Mn⁴⁺ I and II sites of the trimer, indicated by the dashed arrow in Fig. 1(b).

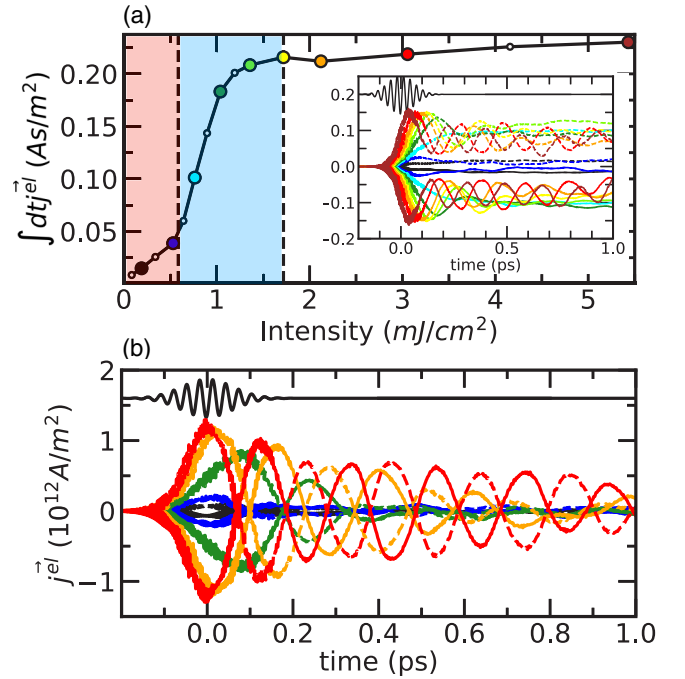


FIG. 2. Generation and evolution of photocurrent (a) integrated current-density $\int dt j^{el}(t)$ versus intensity I showing three regions, namely, I (red shaded), II (blue shaded), and III (white shaded) with distinct photocurrent behavior for light polarized along the \vec{a} direction. Time integration is performed from the beginning until the first $\int dt \vec{j}^{el}(t)$ peak. The inset shows the integrated current $\int dt j^{el}(t)$ versus time t . The symbol colors (except white) of the main figure and the line colors in the inset represent the same light intensities. (b) Instantaneous current $j^{el}(t)$ versus time t . The light pulse is shown in black at the top. The solid and dashed lines in the inset of (a) and (b) show the direction $(\vec{a} + \vec{b})$ and $(\vec{a} - \vec{b})$, respectively, of the current. The colors refer to the increasing intensities with $A_o = 0.15 \hbar/ea_o$ (black), $0.25 \hbar/ea_o$ (blue), $0.35 \hbar/ea_o$ (green), $0.50 \hbar/ea_o$ (orange), and $0.60 \hbar/ea_o$ (red). The corresponding light intensities are $I = 0.19$ mJ/cm² (black), 0.53 mJ/cm² (blue), 1.04 mJ/cm² (green), 2.12 mJ/cm² (orange), and 3.05 mJ/cm² (red).

Oscillations in the instantaneous current over a 200-fs timescale, which are driven by phonons, are already discernible in region I. These oscillations do not contribute to the net time-integrated current; to remove their contribution, we plot only the time-integrated current $\int dt j^{el}(t)$ in the current versus intensity plot [Fig. 2(a)]. Due to the strong el-ph coupling, the octahedral phonon modes follow the photoinduced alterations in the charge disproportionation between Mn sites. Oxygen octahedra around Mn³⁺ sites, originally expanded in the ground state [Fig. 1(a)], start to shrink on photoexcitation, as indicated by decreased O-O bond distances $d_{||}$ along the local trimer axes in Fig. 3(a). In contrast, the average O-O bond lengths in the ab plane around Mn⁴⁺ II and III sites increase as shown in Fig. 3(b). As soon as the octahedral deformations around Mn sites adapt to the new local charge densities, the coherent phonon modes of THz frequencies are excited. The amplitude of the excited phonon modes grows with the light intensity.

In the intensity region II [Fig. 2(a)], the current sharply increases due to a photoinduced magnetic phase transition

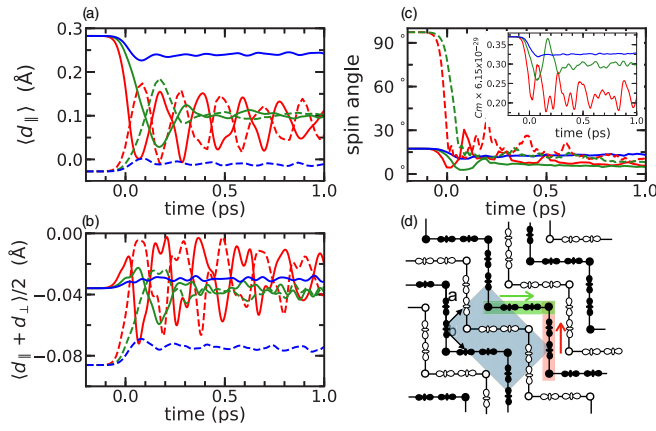


FIG. 3. Dissipation of the excited-electron energy into the octahedral phonon modes and t_{2g} spins. (a) O-O bond expansions d_{\parallel} [see Fig. 1(c)] along the local trimer axes around Mn^{3+} (solid lines); Mn^{4+} I (dashed-lines). (b) Average O-O bond expansion $d_{\parallel ab} = \langle \frac{d_{\parallel} + d_{\perp}}{2} \rangle$ around Mn^{4+} II (solid lines) and Mn^{4+} III sites (dashed lines). (c) Evolution of the average intratrimer spin angles (solid lines) and intertrimer spin angle along the direction of trimer (thick lines). The inset shows the evolution of average local dipole moment $P_l = \langle \sum_i \rho_i \vec{r}_i \rangle$ of tetramer units, indicated in red and green in panel (d). The colored lines refer to the increasing intensities with 0.53 mJ/cm^2 (blue), 1.04 mJ/cm^2 (green), and 3.05 mJ/cm^2 (red). (d) Photo-induced collinear SO in the ab plane. Spin-up (spin-down) sites are indicated in white (black). The ab planes are antiferromagnetically coupled in the \vec{c} direction.

from the original noncollinear SO to a new collinear SO, signaling a departure from the regime of perturbative BPVE. In the new collinear SO, t_{2g} spins on Mn^{4+} III sites rotate to bridge spin-aligned trimers, originally disconnected in the ground state, forming continuous ferromagnetic zigzag chains in the ab plane, consisting of collinear horizontal and vertical Mn-tetramers, as shown in Fig. 3(d). The evolution of the t_{2g} -spin angles between sites is shown in Fig. 3(c).

The electron transfer within tetramers is sensitive to the local orbital polarization and the onsite e_g -orbital energy levels at Mn sites, which in turn depend on the phonon dynamics. As long as there is a charge disproportion between sites within the tetramers, the phonon modes track the local charge asymmetries over time, as shown in the inset of Fig. 3(c), and contribute to phonon-induced photocurrent oscillations. These oscillations decay on subpicosecond timescales primarily due to energy loss to spin degrees of freedom.

On further increase in intensity (region III), the current starts saturating due to the dissipation of excited electron energy into phonon modes. As seen in Figs. 3(a) and 3(b), phonon-induced current oscillations grow in amplitude in region III. Further energy loss from the phonon modes into spin degrees of freedom is also evident from the subpicosecond decay of phonon oscillations in Figs. 3(a) and 3(b). A secondary effect is the change in the electronic structure resulting from excited phonon modes. On photoexcitation in region III, the energy gap between the valence and the conduction bands is reduced. This detunes the resonance between the light field and the peak absorption energy, which reduces the absorption coefficient and photocurrent at high intensities.

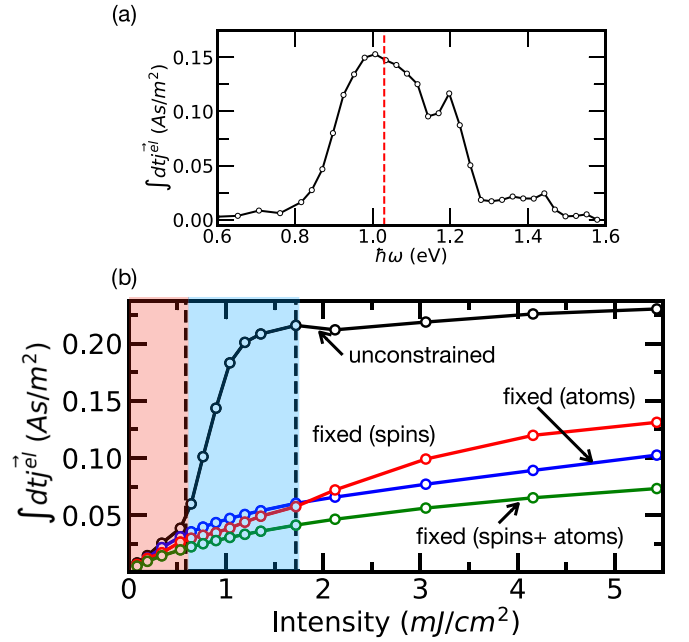


FIG. 4. Photocurrent varying with energy and intensity. (a) Integrated current-density [$\int dt j^{el}(t)$] versus energy showing maximum current around 1.0 eV. The red-dashed line at $\hbar\omega = 1.03 \text{ eV}$ is the energy where the system shows maximum absorption. (b) Integrated current-density [$\int dt j^{el}(t)$] versus intensity for the unconstrained and constrained cases. The unconstrained case shows three different intensity regions, i.e., I (red shaded), II (blue shaded), and III (white shaded), with distinct current behavior.

The photocurrent versus energy shows a peak at $\hbar\omega_p = 1.0 \text{ eV}$, as shown in Fig. 4(a). This peak energy is close to the energy $\hbar\omega_o = 1.03 \text{ eV}$ corresponding to maximum absorption. Overall, the magnetic phase transition results in an enhancement of photocurrent compared with other materials that display BPVE in the perturbative limit. The photoresponsivity $R_p = \frac{1}{I} \int j^{el}(t) dt$, calculated for intensity $I = 1.72 \text{ mJ/cm}^2$ at the time of current saturation in region III, is 12.5 mA/W , an order of magnitude higher than the photoresponsivity for the known ferroelectric oxide BiFeO_3 [14].

In real materials, there are several possible factors that can affect energy dissipation and relaxation processes, such as relaxation due to intrinsic impurities and energy dissipation from the laser illuminated area via heat conduction. Studying these relaxation effects is beyond the scope of our current work. However, such effects can be accommodated in tight-binding models by adding extra terms. For example, the heat conduction into the environment could be taken into account in our model by including a finite friction in the equation of motion of the atoms. For the intrinsic impurities that directly affect the equilibration of the electronic subsystem, a similar damping term can be added for the electronic degrees of freedom.

C. Shift and ballistic current contribution

To measure the contribution of the phonon- and spin-assisted processes, we repeat the simulations keeping either

atoms or spins or both fixed (Fig. 4). With constrained spins, there is clearly no photoinduced magnetic phase transition. Moreover, with fixed atoms, we do not find any magnetic phase transitions either, for the light intensity range covered in the present work, suggesting that phonon dynamics is crucial for the phase transition. This is because the photoinduced octahedral deformations bring $|w_1\rangle$, $|w_2\rangle$, and $|w_6\rangle$ states, involved in the $|w_1\rangle-|w_6\rangle$ and $|w_2\rangle-|w_6\rangle$ hybridization, energetically closer, strengthening the intersite coupling between Mn^{4+} II and III sites [see solid arrow in Fig. 1(b)], thus facilitating the magnetic phase transition. The photocurrent in the cases with constrained atoms or spins grows nonlinearly over the entire intensity range, suggesting a departure from pure shift current contributions as discussed in Ref. [22]. In all of these cases, the direction of current during the light pulse remains predominantly along the bulk polarization direction.

In the absence of spin and lattice dynamics, the photocurrent can only have contributions from the shift current and ballistic current induced by electron-hole excitations, which in Ref. [42] is called the injection current. While injection currents are only present under circularly polarized light in the independent particle picture, the presence of electron-electron interactions allows for these electron-hole pair-induced ballistic or injection currents under linearly polarized light.

In these simulations, because of the finite value of light intensity resulting in finite carrier populations, the shift current contains an excitation component as well as a recombination component (see Supplemental Material for details [39]). Previous *ab-initio* simulations using perturbation theory [15] have treated the fast relaxation limit (where light intensity is weak compared with carrier scattering), where only the excitation component is expected to dominate and scale linearly with the intensity. In contrast, in the slow relaxation limit, the excitation current cancels the recombination current, resulting in vanishing total shift current [43].

In the slow relaxation limit, ballistic currents are expected to scale as the square root of the intensity [43]. We find that our photocurrents in the constrained calculations scale in this manner (Fig. 4), showing that our simulations are performed in this limit where the ballistic currents induced by phonons, spins, and electron-hole pairs are larger than shift currents [43].

III. DISCUSSION

Our study suggests three intensity regions with different current behaviors. In region I with low intensities, lowest order BPVE is active; the linear dependence of current on intensity shows that processes that are second order in the electric field, namely, shift and ballistic photocurrents, contribute to the photocurrent. In the new collinear SO after photo-induced magnetic phase transition in region II of intermediate intensity, the CO within tetramer lacks an inversion center causing asymmetric intersite electron transfer between the original trimer and the adjacent Mn^{4+} III site. As a result of this new ferromagnetic alignment in the noncentrosymmetric *ab* plane, carrier transport is enhanced with the photocurrent being predominantly in the \vec{a} direction.

The mechanism for the magnetic phase transition in the present case can be understood as follows. The photo-induced intersite electron transfer between the Mn^{4+} II and the III sites via $|w_1\rangle-|w_6\rangle$ and $|w_2\rangle-|w_6\rangle$ hybridization, along the trimer axes (shown by the solid black arrow in Fig. 1(b)) triggers spin dynamics. This intersite electron transfer is restricted to the ferromagnetic spin component. This spin-restricted electron transfer changes the local e_g -electrons spin and perturbs the t_{2g} spins due to Hund's coupling, inducing the t_{2g} -spin dynamics. Above a critical intensity $I_o = 0.60 \text{ mJ/cm}^2$, the perturbation on the t_{2g} spins is strong enough to induce a magnetic phase transition within 100 fs. The spin angle fluctuations settle within 500 fs, as shown in Fig. 3(c).

Several past experimental studies have revealed photoinduced phase transitions in the manganite family [44–50]. For example, the study by Li *et al.* shows a photo-induced ferromagnetic state above a threshold light intensity. Most of these reported magnetic phase transitions are accompanied by structural phase transitions driven by photo-induced melting of the ground-state CO and OO. Similarly to these systems, our calculations also predict melting of the original CO and OO, although at intensities above the threshold intensity of the magnetic phase transition. The bulk polarization and the improper ferroelectricity vanish with the melting of the CO and OO. This is similar to the photoinduced nonpolar phases theoretically predicted in the proper ferroelectric barium and lead titanates [51].

In our constrained calculation, where we keep one or more degrees of freedom fixed, we see that both phonons and spins act to increase the overall photocurrent significantly, even in this perturbative limit, with the spin-assisted processes doubling the current of the fully constrained case. This is in contrast to materials systems where the phonon subsystem is only weakly interacting with the electrons, where the phonon-induced ballistic currents are expected to be small [42]. Instead, in the phase-change manganites studied here, the strong electron-phonon coupling in the vicinity of the phase transition enhanced the magnitudes of the phonon-induced ballistic currents. At low light intensities (region I), the spin contribution to the current exceeds the phonon contribution. However, for higher intensities, the phonon-assisted ballistic current becomes larger compared with its spin counterpart. In the absence of phonon dynamics, as for the fixed (atom) case, the excited electrons dissipate energy directly into the spins generating the spin-assisted ballistic current; see Fig. 4(b).

Our results highlight the significance of the photoinduced effects driven by spin and lattice dynamics in BPVE, suggesting the potential for controlling photovoltaic materials responses with tunable excitations and interactions. A design strategy for large BPVE suggested by these results is to look for systems with strong correlations that can undergo optically induced phase transitions at low intensities producing an abrupt change in the photocurrent like in the case studied here. Compared with other nonpolar modes, the electronic properties in complex oxides are strongly linked to the JT distortions. Our study reveals that the coherent dynamics of the excited JT and breathing modes contribute to the phonon-assisted ballistic current. Transition metal oxides such as manganites or nickelates, with SOs in ground and excited states,

are candidates to show spin-assisted BPVE as demonstrated here.

IV. CONCLUSION

We have shown how a combination of spin- and phonon-induced processes can substantially enhance the BPVE using a nonperturbative methodology. The real-time simulations of a strongly correlated system show that photoinduced phase transitions, which are generally ignored in perturbative theoretical methods, significantly impact the photocurrent generation and its evolution. Understanding the effect of the transient spin and lattice dynamics on the dynamical nature of the band structure can be exploited for desirable photovoltaic properties by tuning the correlations and interactions in correlated systems through targeted materials design.

ACKNOWLEDGMENTS

This work was primarily supported by the Computational Materials Sciences Program funded by the U.S. Department of Energy, Office of Science, Basic Energy Sciences, Materials Sciences and Engineering Division. Additional support for tight-binding models were provided through a user project of the Molecular Foundry, a DOE Office of Science User Facility supported by the Office of Science of the U.S. Department of Energy under Contract No. DE-AC02-05CH11231. Part of the work was performed under the auspices of the U.S. Department of Energy by Lawrence Livermore National Laboratory under Contract No. DE-AC52-07NA27344. This research used resources of the National Energy Research Scientific Computing Center, a DOE Office of Science User Facility supported by the Office of Science of the U.S. Department of Energy under Contract No. DE-AC02-05CH11231.

APPENDIX: METHODOLOGY

We use the Ehrenfest dynamics with a tight-binding model to study the optical excitation and its evolution. The complete model with its parameters has been discussed in detail in our previous work [35]. Details about the implementation of the Ehrenfest dynamics are presented in Ref. [36].

1. Tight-binding model

The total potential energy functional of the system (details in Ref. [35]), as already defined in Eq. (1), is

$$E_{\text{pot}}(|\psi_n\rangle, \vec{S}_R, Q_{i,R}) = E_e(|\psi_n\rangle) + E_S(\vec{S}_R) + E_{\text{ph}}(Q_{i,R}) + E_{e-\text{ph}}(|\psi_n\rangle, Q_{i,R}) + E_{e-S}(|\psi_n\rangle, \vec{S}_R). \quad (\text{A1})$$

The electronic energy $E_e = E_{\text{kin}} + E_U$ of the system consists of kinetic energy and el-el interaction. The kinetic energy of the e_g electrons is

$$E_{\text{kin}} = \sum_{R,R'} \sum_n f_n \sum_{\sigma} \sum_{\alpha,\beta} \psi_{\sigma,\alpha,R,n}^* T_{\alpha,\beta,R,R'} \psi_{\sigma,\beta,R',n}. \quad (\text{A2})$$

The hopping-matrix elements contribute only onsite and nearest-neighbor terms between the Mn sites. The hopping matrix \mathbf{T} elements are defined in Ref. [35].

The onsite Coulomb energy between e_g electrons

$$E_U = \frac{1}{2}(U - 3J_{xc}) \sum_R \left(\sum_{\sigma,\alpha} \rho_{\sigma,\alpha,\sigma,\alpha,R} \right)^2 - \frac{1}{2}(U - 3J_{xc}) \sum_R \sum_{\sigma,\alpha,\sigma',\beta} |\rho_{\sigma,\alpha,\sigma',\beta,R}|^2 + \frac{1}{2}J_{xc} \sum_R \sum_{\sigma,\sigma'} (-1)^{\sigma-\sigma'} \sum_{k \in \{x,z\}} \times \left[\left(\sum_{\alpha,\beta} \rho_{\sigma,\alpha,\sigma',\beta,R} \sigma_{\beta\alpha}^{(k)} \right) \left(\sum_{\alpha,\beta} \rho_{-\sigma,\alpha,-\sigma',\beta,R} \sigma_{\beta\alpha}^{(k)} \right) + \left(\sum_{\alpha} \rho_{\sigma,\alpha,\sigma',\alpha,R} \right) \left(\sum_{\alpha} \rho_{-\sigma,\alpha,-\sigma',\alpha,R} \right) \right]. \quad (\text{A3})$$

The first and the second terms in the E_U expression are the Hatree and the corresponding self-interaction correction. Here $\rho_{\sigma,\alpha,\sigma',\beta,R}$ are the local one-center reduced density matrix; $\sigma_{\alpha\beta}^{(k)}$ indicates the three Pauli matrices for $k \in \{x, y, z\}$. The notation $-\sigma$ implies $-\sigma = \uparrow$ for $\sigma = \downarrow$ and vice versa. Similarly, $(-1)^{\sigma-\sigma'} = 1$ for $\sigma = \sigma'$ and $(-1)^{\sigma-\sigma'} = -1$ for $\sigma \neq \sigma'$.

The electron-phonon coupling E_{e-ph} is

$$E_{e-ph} = g_{JT} \sum_{R,\sigma} \sum_{\alpha,\beta} \rho_{\sigma,\alpha,\sigma,\beta,R} M_{\beta,\alpha}^Q(Q_{1,R}, Q_{2,R}, Q_{3,R}), \quad (\text{A4})$$

where g_{JT} and g_{br} are the electron-phonon coupling constants and

$$M^Q(Q_1, Q_2, Q_3) = \begin{pmatrix} Q_3 & Q_2 \\ Q_2 & -Q_3 \end{pmatrix} - \mathbf{1} \frac{g_{br}}{g_{JT}} Q_1. \quad (\text{A5})$$

We include three octahedral phonon modes in our model, two JT ($Q_{2,R}$ and $Q_{3,R}$), and a breathing $Q_{1,R}$ [52]. These phonon modes are defined as

$$Q_{1,R} = \frac{1}{\sqrt{3}}(d_{x,R} + d_{y,R} + d_{z,R} - 3\bar{d}) \quad (\text{A6})$$

$$Q_{2,R} = \frac{1}{\sqrt{2}}(d_{x,R} - d_{y,R}) \quad (\text{A7})$$

$$Q_{3,R} = \frac{1}{\sqrt{6}}(2d_{z,R} - d_{x,R} - d_{y,R}), \quad (\text{A8})$$

where $d_{x,R}$, $d_{y,R}$, and $d_{z,R}$ denote the O-O distances along the x , y , and z directions, respectively, surrounding the Mn site R ; $\bar{d} = 3.845 \text{ \AA}$ is the equilibrium O-O distance.

The phonon energy E_{ph} describes the term restoring the symmetric octahedron

$$E_{\text{ph}} = \frac{1}{2}k_{JT} \sum_R (Q_{2,R}^2 + Q_{3,R}^2) + \frac{1}{2}k_{br} \sum_R Q_{1,R}^2, \quad (\text{A9})$$

where k_{JT} is the restoring force constant for the JT distortions and k_{br} is the restoring force constant of the breathing distortion.

We describe the three majority-spin t_{2g} electrons at site R by their classical spin \vec{S}_R . While the direction of the spin may vary, the magnitude of the spin vector is fixed to $|\vec{S}_R| = \frac{3}{2}\hbar$.

TABLE I. Parameters for the tight-binding model. For detailed information about the extraction of these model parameters from the first-principles studies, see Ref. [35].

J_H	0.653 eV	g_{br}	2.988 eV/Å
U	2.514 eV	k_{br}	9.04 eV/Å ²
J_{xc}	0.692 eV	J_{AF}	0.014 eV
g_{JT}	2.113 eV/Å	t_{hop}	0.585 eV
k_{JT}	5.173 eV/Å ²	\bar{d}	1.923 Å

The spin energy

$$E_S = \frac{1}{2} J_{AF} \sum_{R,R'} \delta_{|\bar{R}-\bar{R}'|-1} \left(\frac{3\hbar}{2} \right)^{-2} \vec{S}_R \vec{S}_{R'} \quad (\text{A10})$$

is due to a small antiferromagnetic coupling of the spins on neighboring sites.

The spins \vec{S}_R of the t_{2g} electrons are strongly coupled to the spins of the e_g electrons by the Hund's coupling J_H . The Hund's coupling is described by

$$E_{e-S} = -J_H \sum_{R,\alpha} \sum_{\sigma,\sigma'} \rho_{\sigma,\alpha,\sigma',\alpha,R} M_{\sigma',\sigma}^S(\vec{S}_R), \quad (\text{A11})$$

where

$$\mathbf{M}^S(\vec{S}) = \left(\frac{3\hbar}{2} \right)^{-1} \begin{pmatrix} S_z & S_x - iS_y \\ S_x + iS_y & -S_z \end{pmatrix}. \quad (\text{A12})$$

The model parameters used in the present work are summarized in Table I.

2. Ehrenfest dynamics

The one-particle wave functions of the e_g electrons evolve according to the time-dependent Schrödinger equation,

$$i\hbar \partial_t \psi_{\sigma,\alpha,R,n} = \frac{\partial E_{\text{pot}}}{\partial \psi_{\sigma,\alpha,R,n}^*}. \quad (\text{A13})$$

TABLE II. Simulation parameters.

k Grid	$1 \times 1 \times 1$
Supercell	$N_x \times N_y \times N_z = 12 \times 12 \times 4$
Mn sites per unit cell	$N_{\text{Mn}} = 576$
O sites per unit cell	$N_O = 1728$
Mn-Mn spacing	$d_{\text{Mn-Mn}} = 3.84 \text{ \AA}$
Time step	$\Delta_t = 0.060 (4\pi\epsilon_0)^2 \hbar^3 / (m_e e^4)$ $= 1.45 \times 10^{-18} \text{ s}$
Oxygen mass	$M_O = 15.998 u$
Photon energy	$\hbar\omega_o = 1.03 \text{ eV}$
Pulse length (FWHM)	$2\sqrt{\ln 2} c_w = 100 \text{ fs}$

The t_{2g} spin at Mn site R with absolute magnetic moment m_S evolves according to the equation

$$i\partial_t S_{i,R} = \frac{2m_S}{\hbar} \left(\frac{3\hbar}{2m_S} \frac{\partial E_{\text{pot}}}{\partial S_{i,R}} \right) \times \vec{S}_R$$

$$i\partial_t \vec{S}_R = \frac{2m_S}{\hbar} \vec{B}_R \times \vec{S}_R, \quad (\text{A14})$$

where $B_{i,R} = \frac{3\hbar}{2m_S} \frac{\partial E_{\text{pot}}}{\partial S_{i,R}}$ is the quasimagnetic field acting at site R due to Hund's coupling with the e_g electrons and the nearest intersite antiferromagnetic interaction. The complete derivation of Eq. (A14) is given in Ref. [37] and also in the Appendix.

Last, the oxygen atoms evolve according to the classical equation of motion

$$M_O \partial_t^2 R_j = - \frac{\partial E_{\text{pot}}}{\partial R_j}. \quad (\text{A15})$$

R_i in the above equation is the structural degrees of freedom of oxygen ions and M_O is their mass. For the complete details of the Ehrenfest dynamics, including the derivation of the above equations and their numerical implementations, see Refs. [36,37]. Table II summarizes the relevant parameters we used for the simulations.

- [1] B. I. Sturman and V. M. Fridkin, *The Photovoltaic and Photo-refractive Effects in Noncentrosymmetric Materials* (Gordon and Breach Science Publishers, Philadelphia, 1992).
- [2] C. Paillard, X. Bai, I. C. Infante, M. Guennou, G. Geneste, M. Alexe, J. Kreisel, and B. Dkhil, *Adv. Mater.* **28**, 5153 (2016).
- [3] A. M. Burger, R. Agarwal, A. Aprelev, E. Schrubba, A. Gutierrez-Perez, V. M. Fridkin, and J. E. Spanier, *Sci. Adv.* **5**, eaau5588 (2019).
- [4] J. E. Moore and J. Orenstein, *Phys. Rev. Lett.* **105**, 026805 (2010).
- [5] I. Sodemann and L. Fu, *Phys. Rev. Lett.* **115**, 216806 (2015).
- [6] Y. Zhang, H. Ishizuka, J. v. d. Brink, C. Felser, B. Yan, and N. Nagaosa, *Phys. Rev. B* **97**, 241118 (2018).
- [7] T. Morimoto and N. Nagaosa, *Sci. Adv.* **2**, e1501524 (2016).
- [8] R. von Baltz and W. Kraut, *Solid State Commun.* **26**, 961 (1978).
- [9] W. Kraut and R. von Baltz, *Phys. Rev. B* **19**, 1548 (1979).
- [10] R. von Baltz and W. Kraut, *Phys. Rev. B* **23**, 5590 (1981).
- [11] H. Presting and R. Von Baltz, *Phys. Status Solidi B* **112**, 559 (1982).
- [12] J. E. Sipe and A. I. Shkrebtii, *Phys. Rev. B* **61**, 5337 (2000).
- [13] S. M. Young and A. M. Rappe, *Phys. Rev. Lett.* **109**, 116601 (2012).
- [14] S. M. Young, F. Zheng, and A. M. Rappe, *Phys. Rev. Lett.* **109**, 236601 (2012).
- [15] L. Z. Tan, F. Zheng, S. M. Young, F. Wang, S. Liu, and A. M. Rappe, *npj Comput. Mater.* **2**, 16026 (2016).
- [16] V. I. Belinicher and B. I. Sturman, *Sov. Phys. Usp.* **23**, 199 (1980).
- [17] B. I. Sturman, *Phys. Usp.* **63**, 407 (2020).
- [18] Z. Dai, A. M. Schankler, L. Gao, L. Z. Tan, and A. M. Rappe, *Phys. Rev. Lett.* **126**, 177403 (2021).
- [19] A. M. Cook, B. M. Fregoso, F. de Juan, S. Coh, and J. E. Moore, *Nat. Commun.* **8**, 14176 (2017).
- [20] S.-J. Gong, F. Zheng, and A. M. Rappe, *Phys. Rev. Lett.* **121**, 017402 (2018).

- [21] B. M. Fregoso, R. A. Muniz, and J. E. Sipe, *Phys. Rev. Lett.* **121**, 176604 (2018).
- [22] T. Barik and J. D. Sau, *Phys. Rev. B* **101**, 045201 (2020).
- [23] R. A. Kaindl, M. A. Carnahan, D. Hägele, R. Löwenich, and D. S. Chemla, *Nature (London)* **423**, 734 (2003).
- [24] S. Leinß, T. Kampfrath, K. v.Volkman, M. Wolf, J. T. Steiner, M. Kira, S. W. Koch, A. Leitenstorfer, and R. Huber, *Phys. Rev. Lett.* **101**, 246401 (2008).
- [25] P. Buczek, A. Ernst, P. Bruno, and L. M. Sandratskii, *Phys. Rev. Lett.* **102**, 247206 (2009).
- [26] G. Fischer, M. Däne, A. Ernst, P. Bruno, M. Lüeders, Z. Szotek, W. Temmerman, and W. Hergert, *Phys. Rev. B* **80**, 014408 (2009).
- [27] C. Verdi, F. Caruso, and F. Giustino, *Nat. Commun.* **8**, 15769 (2017).
- [28] T. Kampfrath, A. Sell, G. Klatt, A. Pashkin, S. Mährlein, T. Dekorsy, M. Wolf, M. Fiebig, A. Leitenstorfer, and R. Huber, *Nat. Photonics* **5**, 31 (2011).
- [29] M. Reticcioli, U. Diebold, G. Kresse, and C. Franchini, *Small Polarons in Transition Metal Oxides, Handbook of Materials Modeling Applications Current and Emerging Materials* (Springer International Publishing, Cham, 2019), pp. 1–39.
- [30] D. Daranciang, M. J. Highland, H. Wen, S. M. Young, N. C. Brandt, H. Y. Hwang, M. Vattilana, M. Nicoul, F. Quirin, J. Goodfellow, T. Qi, I. Grinberg, D. M. Fritz, M. Cammarata, D. Zhu, H. T. Lemke, D. A. Walko, E. M. Dufresne, Y. Li, J. Larsson *et al.*, *Phys. Rev. Lett.* **108**, 087601 (2012).
- [31] S. Priyadarshi, K. Pierz, and M. Bieler, *Phys. Rev. Lett.* **109**, 216601 (2012).
- [32] S. Mori, C. H. Chen, and S.-W. Cheong, *Nature (London)* **392**, 473 (1998).
- [33] P. G. Radaelli, G. Iannone, M. Marezio, H. Y. Hwang, S.-W. Cheong, J. D. Jorgensen, and D. N. Argyriou, *Phys. Rev. B* **56**, 8265 (1997).
- [34] M. T. Fernández-Díaz, J. L. Martínez, J. M. Alonso, and E. Herrero, *Phys. Rev. B* **59**, 1277 (1999).
- [35] M. Sotoudeh, S. Rajpurohit, P. Blöchl, D. Mierwaldt, J. Norpoth, V. Roddatis, S. Mildner, B. Kressdorf, B. Iffland, and C. Jooss, *Phys. Rev. B* **95**, 235150 (2017).
- [36] S. Rajpurohit, C. Jooss, and P. E. Blöchl, *Phys. Rev. B* **102**, 014302 (2020).
- [37] S. Rajpurohit, L. Z. Tan, C. Jooss, and P. E. Blöchl, *Phys. Rev. B* **102**, 174430 (2020).
- [38] T. Hotta and E. Dagotto, [arXiv:cond-mat/0212466](https://arxiv.org/abs/cond-mat/0212466) [cond-mat.str-el].
- [39] See Supplemental Material at <http://link.aps.org/supplemental/10.1103/PhysRevB.105.094307> for details, which includes Refs [22,36,53,54].
- [40] R. Peierls, *Z. Phys.* **80**, 763 (1933).
- [41] T. N. Todorov, D. Dundas, J.-T. Lü, M. Brandbyge, and P. Hedegård, *Eur. J. Phys.* **35**, 065004 (2014).
- [42] T. Kaneko, Z. Sun, Y. Murakami, D. Golež, and A. J. Millis, *Phys. Rev. Lett.* **127**, 127402 (2021).
- [43] O. Matsyshyn, F. Piazza, R. Moessner, and I. Sodemann, *Phys. Rev. Lett.* **127**, 126604 (2021).
- [44] K. Miyano, T. Tonogai, T. Satoh, H. Oshima, and Y. Tokura, *J. Phys. IV France* **09**, Pr10-311 (1999).
- [45] M. Matsubara, Y. Okimoto, T. Ogasawara, Y. Tomioka, H. Okamoto, and Y. Tokura, *Phys. Rev. Lett.* **99**, 207401 (2007).
- [46] D. Polli, M. Rini, S. Wall, R. W. Schoenlein, Y. Tomioka, Y. Tokura, G. Cerullo, and A. Cavalleri, *Nat. Mater.* **6**, 643 (2007).
- [47] T. Mizokawa, *Nanoscale Res. Lett.* **7**, 582 (2012).
- [48] T. Li, A. Patz, L. Mouchliadis, J. Yan, T. A. Lograsso, I. E. Perakis, and J. Wang, *Nature (London)* **496**, 69 (2013).
- [49] P. Beaud, A. Caviezel, S. O. Mariager, L. Rettig, G. Ingold, C. Dornes, S.-W. Huang, J. A. Johnson, M. Radovic, T. Huber, T. Kubacka, A. Ferrer, H. T. Lemke, M. Chollet, D. Zhu, J. M. Glownia, M. Sikorski, A. Robert, H. Wadati, M. Nakamura *et al.*, *Nat. Mater.* **13**, 923 (2014).
- [50] H. Lin, H. Liu, L. Lin, S. Dong, H. Chen, Y. Bai, T. Miao, Y. Yu, W. Yu, J. Tang, Y. Zhu, Y. Kou, J. Niu, Z. Cheng, J. Xiao, W. Wang, E. Dagotto, L. Yin, and J. Shen, *Phys. Rev. Lett.* **120**, 267202 (2018).
- [51] C. Paillard, E. Torun, L. Wirtz, J. Íñiguez, and L. Bellaiche, *Phys. Rev. Lett.* **123**, 087601 (2019).
- [52] J. Kanamori, *J. Appl. Phys.* **31**, S14 (1960).
- [53] B. M. Fregoso, T. Morimoto, and J. E. Moore, *Phys. Rev. B* **96**, 075421 (2017).
- [54] M. J. Rice and E. J. Mele, *Phys. Rev. Lett.* **49**, 1455 (1982).